Simulating the extended Su-Schrieffer-Heeger model and transferring an entangled state based on a hybrid cavity-magnon array

Da-Wei Wang, Chengsong Zhao, Junya Yang, Ye-Ting Yan, and Ling Zhou ⬤[*]

School of Physics, Dalian University of Technology, Dalian 116024, People's Republic of China

We propose a scheme to simulate the extended Su-Schrieffer-Heeger (SSH) model by using the hybrid cavity magnonics system. We consider a hybrid cavity-magnon array with N sites, where each site contains two cavity modes and one magnon mode, and the cavity modes at the neighboring site couple to each other with controllable tunneling rates. Under large detuning conditions, we adiabatically eliminate the cavity field and obtain periodic interactions between the magnons depending on the phase between adjacent cavity fields. After setting the relationship of the phases, we obtain the magnon version of the extended SSH model. Employing this model, we investigate the distribution of edge states and the topological phase transition. Moreover, our scheme can be easily extended to the SSHm model with the jump period m by setting different phase shifts. Finally, considering the noninteger cell case, we find that an arbitrary magnon entangled state can be encoded by two edge states and transferred from the left site end to the right site end via the adiabatic channel. Our work provides a pathway for realizing quantum information transmission and offers an idea for implementing quantum simulations based on cavity magnonics systems.

I. INTRODUCTION

Magnons offer a promising architecture for quantum information processing due to their low damping rate, high frequency tunability, and excellent compatibility [1–5]. Magnons can couple with a wide range of fields such as coupling with microwaves and optical photons via the magnon dipole [6,7] and via the magnon-optical Faraday effect [8–10], as well as interacting with the phonon by magnon-elastic effect [11,12]. Taking advantage of the coherent coupling of magnons with different types of quantum systems, hybrid magnon systems have attracted much attention in recent years [13–19].

The cavity magnonics system generally consists of single crystal yttrium iron garnet (YIG) spheres and a high Q cavity. The Kittle modes of the spin ensemble (ground state) in YIG spheres can be coupled with microwave cavity mode. In particular, the coupling between magnon mode and microwave cavity mode can reach the region of strong coupling or even ultrastrong coupling due to the high spin density and the exchange between spins [6,7,20]. A number of interesting phenomena have been demonstrated in the cavity magnon system, such as magnon-induced nonreciprocity [16,21,22], magnon dark modes [13,23], magnon blockades [24,25], magnon entanglement and steering [26,27], magnon lasers [28], high-order sidebands [29], and quantum simulation [30,31].

With many interesting features including robustness to local decoherence processes and potential applications in quantum information, topological insulators have received

much interest and attention in quantum physics [32–35]. Originally used to describe the transport properties of conducting polyacetylene [36,37], the Su-Schrieffer-Heeger (SSH) model has recently attracted increasing attention due to its simplest topological insulator model with a simple structure and abundant physical images [34,38–41]. A series of generalizations by increasing the period of the hopping model are often referred to as the extensions of the SSH model. Here, we refer to the extended SSH models with hopping coefficients of period three and period four as the SSH3 [42–44], and SSH4 models [45,46], respectively. As an extension of the SSH model, the SSH3 model exhibits interesting features that are different from those of the SSH model, such as more edge states [42,43], absence of symmetry [47], etc. Several recent works have shown that even in the absence of chiral and mirror symmetry, the bulk-edge correspondence can also be established due to the fact that this model possesses point-chiral symmetry [48,49]. Based on the bulk-edge correspondence, nonzero bulk topological invariants predict the appearance of local modes at the edges of the chain [50]. The special edge states are protected by the energy gap of the topological system, resulting in edge states that are insensitive by local disorder and perturbations [32,33,51]. More importantly, topologically protected edge states can be used for robust disordered photon and phonon transport [52,53]. This means that new pathways are available for quantum information processing based on topological edge channels.

As more attention has been paid to the extended SSH model, it has been proposed to simulate the extended SSH model with different platforms such as optical systems [54,55], atomic chains [43,56], photonic lattice [57], and microelectromechanical systems [58]. However, few studies have used cavity magnon systems to simulate the extended
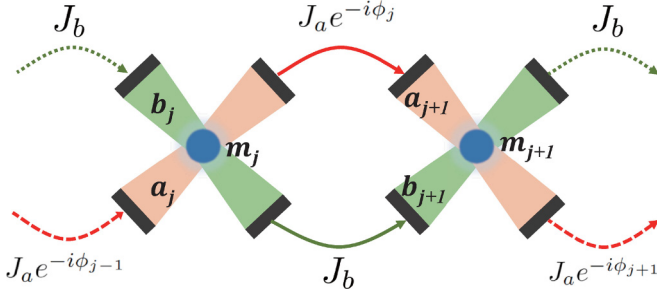

FIG. 1. Schematic illustration of a one-dimensional cavity magnon array. The magnon mode m_j (blue) couples to two cavity modes a_j (pink), b_j (green) with coupling strengths g_a, g_b. The jumping rates between neighbor cavity b is J_b, while the hopping from cavity a_j to a_{j+1} is $J_a e^{-i\phi_j}$.

SSH model. Given the advantages of the cavity magnon system, in this paper, we present a scheme for the simulation of the extended SSH model using hybrid cavity magnon systems. We consider a set of hybrid cavity magnon arrays with N sites, where each site contains two cavity modes and one magnon mode, and the jumping between sites is real or complex photon tunneling. Under large detuning conditions, we adiabatically eliminate the cavity field and obtain periodic interactions between the magnons. That interaction between the magnons mediated by the cavity field depends on the phase between adjacent cavity fields. After setting the relationship of the phases, we achieve the superlattice structure of the magnons. Then, we simulate the magnon version of the extended SSH model and study the distribution of the edge states of the system as well as the topological phase transition. Finally, considering the case of noninteger cells, we discuss the transfer of magnon entangled states, and the results show that entangled states can be transferred by slowly and adiabatically changing the phase between the neighboring cavity fields. Furthermore, an arbitrary information encode in edge state can be transmission through the array.

II. MODEL AND HAMILTONIAN

We consider a one-dimensional cavity magnon array, in which each YIG sphere couples with two cavity fields as shown in Fig. 1. The cavity modes at the neighbor site couple each other with tunneling rates J_a, J_b. Then, the Hamiltonian of the system can be written as

$$H = H_c + H_{om} + H_{hop}, \qquad (1)$$

where

$$H_c = \sum_{j=1}^{N} \omega_{a,j} a_j^\dagger a_j + \omega_{b,j} b_j^\dagger b_j + \omega_{m,j} m_j^\dagger m_j,$$

$$H_{om} = \sum_{j=1}^{N} (g_a a_j^\dagger + g_b b_j^\dagger) m_j + \text{H.c.},$$

$$H_{hop} = \sum_{j=1}^{N} J_a a_{j+1}^\dagger a_j e^{-i\phi_j} + J_b b_{j+1}^\dagger b_j + \text{H.c.}. \qquad (2)$$

H_c is the free energy of the two microwave fields and magnon mode with frequencies $\omega_{a,j}$ ($\omega_{b,j}$) and $\omega_{m,j}$, respectively, where $a_j^\dagger$ and a_j ($b_j^\dagger$ and b_j), $m_j^\dagger$ and m_j are the creation and annihilation operators of the two cavity fields and the magnon. H_{om} represents the magnon mode coupling with the cavity fields with strengths g_a (g_b). H_{hop} is interpreted as the jumping between adjacent cavities with strength J_a and J_b, respectively. Moreover, for cavity a_j, the photon tunneling between nearest neighbor is complex with the phase factor ϕ_j. Recently, a number of theoretical proposals [59–61] and experiments [62,63] have also been used to implement complex photon tunneling. For simplicity, we set $\omega_{a,j} = \omega_a$, $\omega_{b,j} = \omega_b$, and $\omega_{m,j} = \omega_m$.

Now, we perform transformation $a_j = c_j e^{i\theta_j}$, then Eq. (2) becomes

$$H_c = \sum_{j=1}^{N} \omega_a c_j^\dagger c_j + \omega_{b,j} b_j^\dagger b_j + \omega_{m,j} m_j^\dagger m_j,$$

$$H_{om} = \sum_{j=1}^{N} (g_a c_j^\dagger e^{-i\theta_j} + g_b b_j^\dagger) m_j + \text{H.c.},$$

$$H_{hop} = \sum_{j=1}^{N} J_a c_{j+1}^\dagger c_j + J_b b_{j+1}^\dagger b_j + \text{H.c.}, \qquad (3)$$

where we set $\phi_j = \theta_j - \theta_{j+1}$. By introducing Fourier transformation $o_j = \frac{1}{\sqrt{N}} \sum_k e^{ikj} o_k$ ($o = c, b$), with $k \in [-\pi, \pi]$, we can diagonalize the Hamiltonian H_{hop}. Then, the total Hamiltonian Eq. (1) can be rewritten as

$$H = \sum_j \omega_m m_j^\dagger m_j$$

$$+ \sum_k [(\omega_a + 2J_a \cos k) c_k^\dagger c_k + (\omega_b + 2J_b \cos k) b_k^\dagger b_k]$$

$$+ \sum_{j,k} \left[\frac{1}{\sqrt{N}} (g_a e^{-i\theta_j} c_k^\dagger + g_b b_k^\dagger) e^{-ikj} m_j + \text{H.c.} \right]. \qquad (4)$$

Assuming that the cavity field is initially in the vacuum state, we can use the Schrieffer-Wolff transformation [64] to adiabatically eliminate the cavity field. The details can be found in the Appendix. After performing this transformation, we can obtain the effective magnon-magnon interaction. Then, the Hamiltonian is reduced to

$$H_S = \sum_j \omega_m m_j^\dagger m_j + \sum_{j,l,k} \frac{1}{N} \left[\left(\frac{g_a^2 e^{i(\theta_j - \theta_l)}}{\Delta_{am} - 2J_a \cos k} \right. \right.$$

$$\left. \left. + \frac{g_b^2}{\Delta_{bm} - 2J_b \cos k} \right) m_j^\dagger m_l e^{i(j-l)k} + \text{H.c.} \right], \qquad (5)$$

where $\Delta_{jm} = \omega_j - \omega_m$ ($j = a, b$) is the detuning between the cavity and magnon. Considering $\Delta_{am} \gg 2J_a \cos k$, $\Delta_{bm} \gg 2J_b \cos k$, and using the Taylor expansion, we can obtain

$$\frac{1}{\Delta_{am} - 2J_a \cos k} = \frac{1}{\Delta_{am}} + \frac{J_a}{\Delta_{am}^2} (e^{ik} + e^{-ik}),$$

$$\frac{1}{\Delta_{bm} - 2J_b \cos k} = \frac{1}{\Delta_{bm}} + \frac{J_b}{\Delta_{bm}^2} (e^{ik} + e^{-ik}). \qquad (6)$$
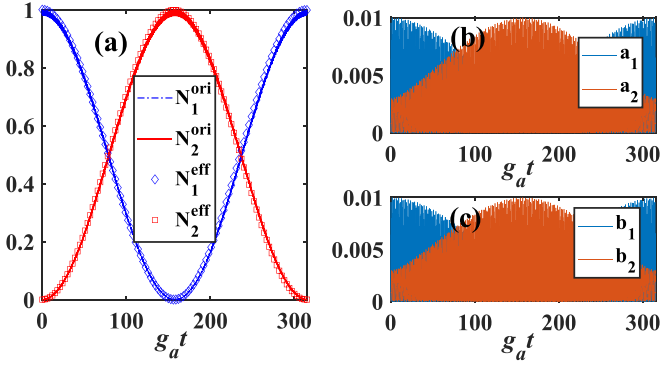
FIG. 2. Numerical comparison of the original Hamiltonian with the effective Hamiltonian. (a) The mean magnon number varying with time. (b and c) The mean photon number as a function of time for cavity a and cavity b, respectively. The parameters are $\phi_1 = \pi/3$, $\omega_a = \omega_b = 100g_a$, $\omega_m = 80g_a$, $J_a = J_b = 2g_a$, and $g_b = g_a$.

Plugging Eq. (6) into Eq. (5), we can obtain the effective Hamiltonian as

$$H_S = \sum_j^N \left(\omega_m + \frac{g_a^2}{\Delta_{am}} + \frac{g_b^2}{\Delta_{bm}} \right) m_j^\dagger m_j$$
$$+ (J_{j,j+1} m_{j+1}^\dagger m_j + \text{H.c.}), \quad (7)$$

where $J_{j,j+1} = \left(\frac{g_a^2 J_a}{\Delta_{am}^2} e^{i\phi_j} + \frac{g_b^2 J_b}{\Delta_{bm}^2} \right)$. The term $\frac{g_a^2}{\Delta_{am}} + \frac{g_b^2}{\Delta_{bm}}$ in the first line of Hamiltonian (7) is the energy shifts for magnon, which is the same for every magnon, so we omit it hereafter. The last term in the above Hamiltonian is effective coupling between adjacent magnons mediated by the cavity modes. The effective coupling stems from two contributions. $\frac{g_a^2 J_a}{\Delta_{am}^2} e^{i\phi_j}$ results from cavity chain a, and $\frac{g_b^2 J_b}{\Delta_{bm}^2}$ originates from cavity chain b. If chain b is absent, $J_{j,j+1} = \frac{g_a^2 J_a}{\Delta_{am}^2} e^{i\phi_j}$, then the phase ϕ_j has no effect on the properties of the system. Once chain b is present, it interferes with chain a, then the phase ϕ_j plays a crucial role in achieving periodic coupling and leads to topological phase transition.

When we consider the loss of the cavity field, we can introduce the non-Hermitian $-\sum_j i\kappa_a a_j^\dagger a_j - i\kappa_b b_j^\dagger b_j$ into Eq. (1), where κ_a and κ_b are the decay rate of the cavity a_j and b_j ($j = 1, 2, 3, \ldots, N$), respectively. With the corresponding calculations, one can obtain a non-Hermitian Hamiltonian. Thus, the current system can be used to simulate in the non-Hermitian topology properties such as non-Hermitian skin effect [65], transport effects [66], directional amplification [67], etc. In this paper, we ignore the effect of cavity field dissipation and concentrate on the simulation of the extend SSH model.

In order to prove the validity of our approximation, now we present numerical simulations by comparing the time evolution governed by effective Hamiltonian Eq. (7) and the full Hamiltonian Eq. (1), respectively. We take two sites as an example. We assume that the first magnon is in the single-excitation state, while all cavities and the second magnon are in vacuum state. In Fig. 2, we plot the mean magnon number N_n ($n = m_1, m_2$) and the mean photon number N_j ($j = a_1, a_2, b_1, b_2$) as a function of time. It can be seen that the
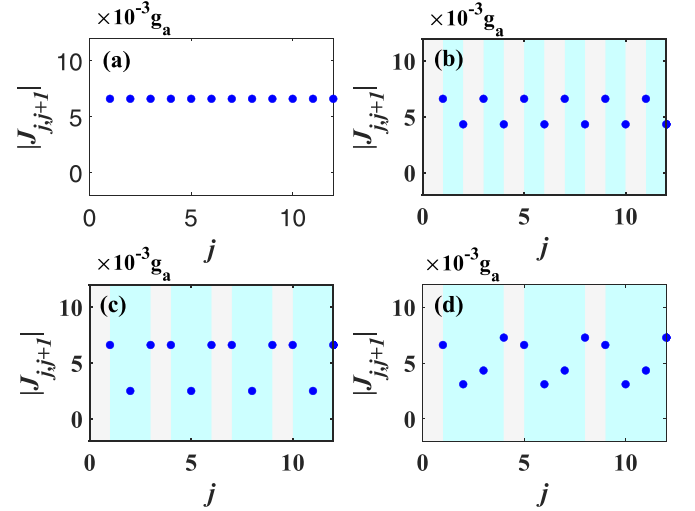

FIG. 3. The distribution of effective coupling $|J_{j,j+1}|$ at the lattice points for different phase shifts: (a) $y = \pi$, (b) $y = \pi/2$, (c) $y = \pi/3$, (d) $y = \pi/4$. The parameters are $\phi_1 = \pi/3$, $\Delta_{am} = \Delta_{am} = 20g_a$, and the other parameters are the same as in Fig. 2.

full Hamiltonian matches well with the effective Hamiltonian. Meanwhile, the population of cavity fields is close to zero, which means that the effective Hamiltonian is trustable.

If we set the phase shift between adjacent phases as a constant, i.e., $\phi_{j+1} - \phi_j = 2y$, then according to the recurrence relation, we can obtain $\phi_j = \phi_1 + 2(j-1)y$, where ϕ_1 denotes the phase of the jumping between the first and second cavity, see Eq. (2). Under this assumption, we can see that the effective coupling depends on the phase shift y and initial phase ϕ_1. In Fig. 3, we plot the distribution of the effective coupling on the lattice points for different phase shifts.

We can see that for the phase shift $y = \pi$, the effective coupling between adjacent magnons is homogeneous as shown in Fig. 3(a). However, for the phase shift $y = \pi/2, \pi/3, \pi/4$ the intensity of the coupling exhibits a periodic variation with a period of 2, 3, 4 sites in the pale blue area of Figs. 3(b), 3(c) and 3(d). For interaction periods of 2, one can implement SSH simulations similar to these works [68–70].

For the phase shift $y = \pi/3$, the effective coupling between adjacent magnons $J_{j,j+1}$ can be simplified as

$$J_{j,j+1} = \begin{cases} J_1 = \frac{g_b^2 J_b}{\Delta_{bm}^2} + \frac{g_a^2 J_a}{\Delta_{am}^2} e^{i\phi_1}, & \mathrm{mod}(j,3) = 1, \\ J_2 = \frac{g_b^2 J_b}{\Delta_{bm}^2} + \frac{g_a^2 J_a}{\Delta_{am}^2} e^{i(\phi_1 + 2\pi/3)}, & \mathrm{mod}(j,3) = 2, \\ J_3 = \frac{g_b^2 J_b}{\Delta_{bm}^2} + \frac{g_a^2 J_a}{\Delta_{am}^2} e^{i(\phi_1 + 4\pi/3)}, & \mathrm{mod}(j,3) = 0, \end{cases}$$
(8)

which clearly shows that the phase ϕ_1 plays an important role in determining J_i ($i = 1, 2, 3$) because of the interference between arrays a and b. In Fig. 4, we plot the variation of the coupling strength between sublattices versus the initial phase for $y = \pi/3$. It can be seen that the absolute values of the coupling coefficients show a periodic variation as ϕ_1 varies and there is a fixed phase difference $2\pi/3$ between them as shown in Fig. 4(a). Similar results can be found for $y = \pi/4$. Therefore, if we consider the minimum repetition
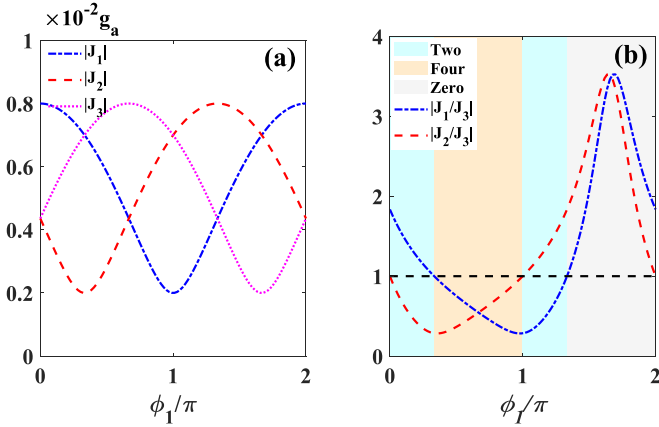
FIG. 4. (a) Coupling strength between sublattices as a function of initial phase for $y = \pi/3$. (b) The ratio of J_1, J_2 to J_3 varies with ϕ_1. The parameters are the same as in Fig. 3 except for $J_b = 1.2$.

period as a unit cell, we can achieve magnon superlattices where the number of sublattices in each cell is more than two by adjusting the phase shift.

III. SIMULATED MAGNON SSH3 MODEL WITH FIXING PHASE SHIFT $y = \pi/3$

As mentioned above, if we choose the phase shift $y = \pi/3$, we can achieve magnon trimer lattice. We draw the diagram of the trimer lattice as shown in Fig. 5, where each cell contains three magnons A, B, and C. In this case, the Hamiltonian (7) becomes

$$H = \sum_j (J_1 m_{A,j}^\dagger m_{B,j} + J_2 m_{B,j}^\dagger m_{C,j}$$
$$+ J_3 m_{C,j}^\dagger m_{A,j+1} + \text{H.c.}), \qquad (9)$$

where J_1 and J_2 are the intracell coupling strength while J_3 is the intercell coupling strength, and J_n ($n = 1, 2, 3$) is given in Eq. (8). The above Hamiltonian is generally also called the SSH3 model [44,49]. Several recent works have pointed out that the SSH3 model can exhibit interesting features that differ from the SSH model, such as more edge states [42,43].

In Fig. 6, we plot the energy spectrum with the variation of initial phase ϕ_1 and the distribution of the band-gap states. We mark the eigenvalues of 20th and 41th in red and the eigenvalues of 21th and 40th in blue. As shown in Fig. 6(a), we can observe that with the changes of ϕ_1, the number of band-gap states also changes. For $\phi_1 = 0$, no band-gap states appear in the energy spectrum. As ϕ_1 increases, the system has a pair of band-gap states with opposite energies. When ϕ_1 is around $\phi_1 = 2\pi/3$, there are four band-gap states. Further
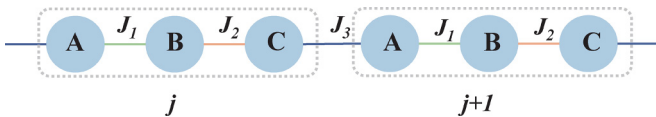

FIG. 5. Schematic illustration of the trimerized lattice model, where J_1, J_2 are the intracell coupling strength and J_3 is the intercell coupling strength.
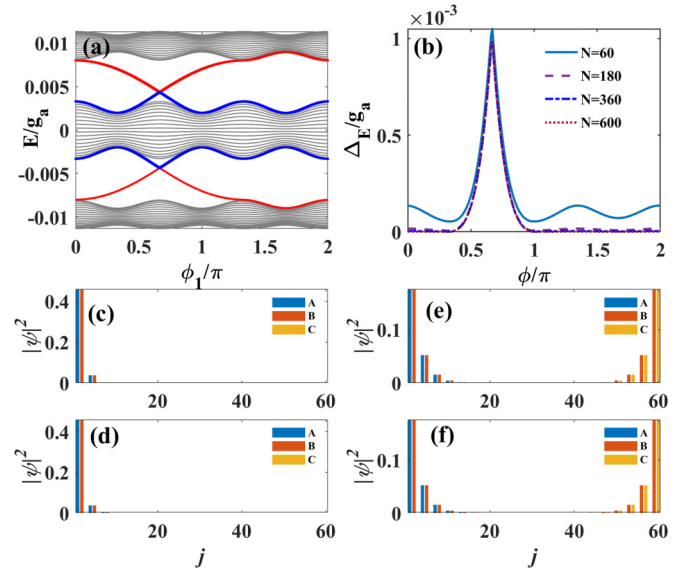

FIG. 6. (a) The energy spectrum with the variation of initial phase ϕ_1. (b) The Δ_E varying with initial phase ϕ_1. (c and d) The probability distribution of the band-gap states associated with the 20th and 41th eigenvalue at the lattice point corresponds to $\phi_1 = \pi/3$. (e and f) The probability distribution of the eigenstates associated with the 20th and 41th eigenvalue corresponds to $\phi_1 = 2\pi/3$. The parameters are the same as in Fig. 4, and $N = 60$.

increases in ϕ_1 will again result in the reappearance of the pair of band-gap states. However, when ϕ_1 is increased to $4\pi/3$ and then further increased, no more band-gap states appear in the energy spectrum.

We now analyze the distribution of the probability of the band-gap state at the lattice points for $N = 60$. For $\phi_1 = \pi/3$, there are two band-gap states corresponding to the 20th and 41th eigenvalue, respectively. Both of them are located on the leftmost side and have the same probability distribution on the sites shown in Figs. 6(c) and 6(d). However, for $\phi_1 = 2\pi/3$, there are four band-gap states in the energy spectrum, which correspond to the 20th, 21th, 40th, and 41th eigenvalue, respectively. The probability distribution of the eigenstates associated with the 20th and 41th eigenvalue is presented in Figs. 6(e) and 6(f).

In addition, at $\phi_1 = 2\pi/3$, the probability distribution of the eigenstate related to the eigenvalue of 20th (21th) is the same as the eigenstate of the eigenvalue of 41th (40th), which we do not display here. This means that eigenstates with the same energy have opposite probability distributions, whereas eigenstates with opposite energies have the same probability distribution. Actually, if we rewrite Eq. (9) as the Bloch Hamiltonian in momentum space, we can find three dispersive bands not symmetric to zero energy, which is similar to Fig. 1(b) in Ref. [49]. This implies that the system has no chiral symmetry [32]. However, the bulk Hamiltonian of SSH3 exhibits a chiral-like symmetry called point chirality, which belongs to the family of particle-hole symmetries [48,49]. The presence of point chirality is what leads to the particular distribution of the eigenstates. The particular distribution of the above band-gap states at the edges is usually referred to as the edge state. According to the bulk-boundary

correspondence in Hermitian systems, nonzero topological invariants imply the existence of edge states of the system exponentially distributed at the boundary under open boundary conditions and vice versa. Therefore, comparing the results for the two different initial phases, we can conclude that a topological phase transition has occurred by changing the initial phase ϕ_1.

Due to size effects, it is difficult to determine the exact number of band-gap states. The main reason stems from the fact that the $N/3$th, $(N/3 + 1)$th, $2N/3$th, and $(2N/3 + 1)$th eigenvalues are very closed to bulk state. We define $\Delta_E = E_{2N/3\text{th}} - E_{(2N/3-1)\text{th}}$ to describe whether the eigenstate corresponding to the $(2N/3)$th eigenvalues is the band-gap state. In Fig. 6(b), we plot the variation of Δ_E with ϕ_1 for different system sizes N. We can see that for $0 < \phi_1 < \pi/3$ and $\pi < \phi_1 < 2\pi$, Δ_E converges to zero, implying that it is not the band-gap state. Moreover, in the range of $2\pi/3 < \phi_1 < \pi$, Δ_E is not zero, which means that the eigenstate corresponding to the $2N/3$th eigenvalues is the band-gap state. Similar results also appear for other eigenvalues.

In addition, we note that at $\phi_1 = \pi/3$, the coupling coefficient satisfies $|J_1| = |J_3| > |J_2|$ for $0 < \phi_1 < \pi/3$, $\{|J_2|, |J_3|\} < |J_1|$, and at $\phi_1 = 2\pi/3$, $|J_1| = |J_2| < |J_3|$ for $\pi/3 < \phi_1 < 2\pi/3$, $\{|J_1|, |J_2|\} < |J_3|$. To facilitate the explanation, we define $x_1 = |J_1/J_3|$, $x_2 = |J_2/J_3|$. Combining the above results with Fig. 4(b), we can find the following relationships. In the range of $\{x_1, x_2\} < 1$, four band-gap states in the energy spectrum relate to the orange area. In the range of $x_1 < 1, x_2 > 1$ or $x_1 > 1, x_2 < 1$, two band-gap states exist, see the sky-blue area. And in other cases, no band-gap state is shown in the gray areas. It is worth noting here that the above statement is only accurate for the long chain limit, and there is an error in the number of band-gap states near the critical value $x_1 = x_2 = 1$ [49].

IV. ENTANGLED STATE TRANSFER BY TOPOLOGICAL EDGE CHANNEL

By comparing the probability distribution of the 20st eigenvalue under different parameters shown in Figs. 6(c) and 6(e), we find the behavior of state transfer. In other words, the probability of being at the leftmost end is partially transferred to the rightmost end. This means that one can implement a topological transfer similar to the scheme proposed in the SSH model [71–73]. For SSH chains with an odd number of sites, there is only one edge state, which is positioned at the left or right of the chain, depending on the ratio of intracell to extracell. Namely, one can adiabatically vary the coupling strength between inside and outside the cell from less than 1 to greater than 1. It is possible to pump the local state from one edge to another, thereby implementing quantum state transfer.

We note that for the present model, the system has four edge states. For all of these band-gap states, with appropriate parameters, we find that those band-gap states can also be localized on the boundary and each edge state can be used as a state transfer channel. However, in order to be able to solve the expressions for the edge states analytically, we choose a noninteger number of cells, $N = 3M - 1$, which means that there are two YIG spheres $m_{A,M}$, $m_{B,M}$ at the end. Under this case, the system has only one pair of band-gap states and the
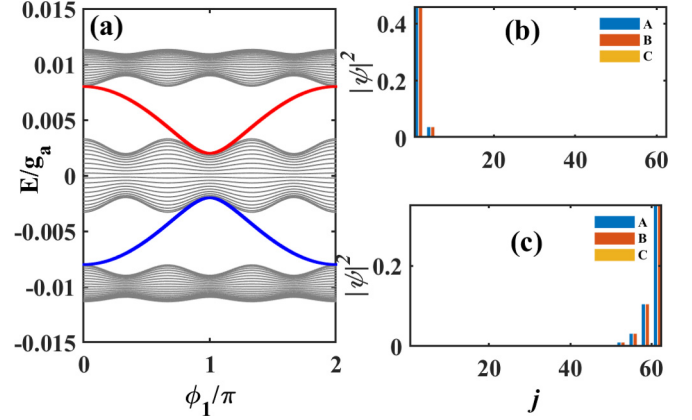

FIG. 7. (a) The energy spectrum varying with initial phase ϕ_1. (b and c) The spatial profile of the band-gap states associated with the 21th eigenvalue at the lattice point corresponds to $\phi_1 = \pi/3$, $\phi_1 = 4/3\pi$. The parameters are the same as in Fig. 4, and $N = 62$.

gap state is fully solvable [74]. For more analysis of edge states, see Refs. [42,43,47].

In Fig. 7(a), we plot the energy spectrum varying with initial phase ϕ_1 for $N = 62$. We can see that as ϕ_1 changes, only two band-gap states exist in the energy gap associated with the 21th and 42th eigenvalue. As shown in Figs. 7(b) and 7(c), we can see that the probability distribution of the two band-gap states corresponding to the 21th eigenvalue moves from the left edge to the right edge with the change of ϕ_1. We note that for the parameters in Figs. 7(b) and 7(c), the distribution of the edge states is not all at the leftmost position, but is also distributed within the second cell. This is due to the distribution of the edge states related to the coupling ratio. We will derive the specific form of the edge state in the following.

In the single-excitation subspace, the wave function of the band-gap state can be written as the following ansatz [71,75]:

$$|\Psi\rangle = \sum_{j=1}^{N} \lambda^j (\alpha m_{A,j}^\dagger + \beta m_{B,j}^\dagger + \gamma m_{C,j}^\dagger) |G\rangle, \tag{10}$$

where $|G\rangle = |00 \dots 0\rangle$ is the ground state of the system and the probability amplitude on site j decays or increases exponentially with increasing distance j. Substituting Eqs. (12) and (9) into the Schrödinger equation, we can obtain

$$E(\alpha m_{A,j}^\dagger + \beta m_{B,j}^\dagger + \gamma m_{C,j}^\dagger) |G\rangle$$
$$= \{(J_1^* \alpha + J_2 \gamma) m_{B,j}^\dagger + (J_1 \beta + J_3^* \gamma \lambda^{-1}) m_{A,j}^\dagger$$
$$+ (J_2^* \beta + \lambda J_3 \alpha) m_{C,j}^\dagger\} |G\rangle. \tag{11}$$

For $3M - 1$ sites, the distribution of the band-gap state has zero probability at lattices C [49]. So, we choose $\gamma = 0$, $J_2^* \beta + \lambda J_3 \alpha = 0$. By solving Eq. (11), we have $|\alpha|^2 = |\beta|^2 = 1/2$, $\lambda = \pm|J_2/J_3|$, and the energy of two edge states $E_\pm = \pm|J_1|$. Finally, we derive the two band-gap state in the single-excitation subspace as follows:

$$|\Psi_\pm\rangle = N_e \sum_{j=1}^{N} \frac{1}{\sqrt{2}} \left| \frac{J_2}{J_3} \right|^j (m_{A,j}^\dagger \pm m_{B,j}^\dagger) |G\rangle, \tag{12}$$
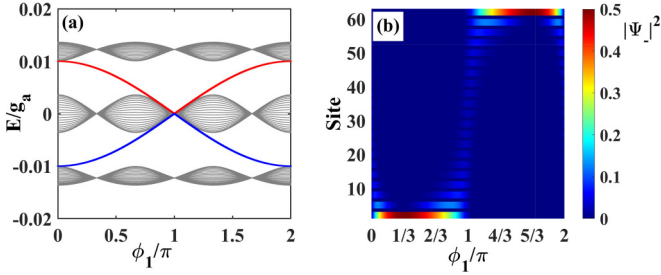
FIG. 8. (a) The energy spectrum varying with the initial phase ϕ_1. (b) The probability distribution of the band-gap states at the lattice point varying with initial phase ϕ_1 associated with the 21th eigenvalue. The parameters are the same as in Fig. 7 except for $J_b = 2g_a$.

where N_e is normalization factor. From the above results, we can see that for $3M - 1$ sites, both the energy and the profile of the band-gap state of the system are closely related to the coupling coefficient as shown in Figs. 7(b) and 7(c). Together with Fig. 4(b), it can be seen that when $\phi_1 \in (0, 2\pi/3)$ with $|J_2/J_3| < 1$ and at $\phi_1 = \pi/3$, the ratio of $|J_2/J_3|$ is the minimum. Meanwhile, when $\phi_1 \in (4\pi/3, 2\pi)$ with $|J_2/J_3| > 1$ and at $\phi_1 = 5\pi/3$, the ratio of $|J_2/J_3|$ is the maximum. Therefore, after the above analysis, we can adiabatically and slowly vary ϕ_1 to achieve quantum state transfer.

We can see that at $\phi_1 = \pi/3$, $|J_2/J_3| \ll 1$, the initial state of the system is $|L_\pm\rangle = \frac{1}{\sqrt{2}}(m^\dagger_{A,1} \pm m^\dagger_{B,1})|G\rangle$ located near the leftmost end, which is an entangled state as well as an edge state. When ϕ_1 adiabatically and slowly changes to some critical value, $\phi_1 = 5\pi/3$, in this case, $|J_2/J_3| \gg 1$, and the final state becomes $|R_\pm\rangle = \frac{1}{\sqrt{2}}(m^\dagger_{A,3M} \pm m^\dagger_{B,3M})|G\rangle$, which is located on the rightmost end. This means that we can achieve entangled state transfer of the magnons by adiabatically and slowly adjusting the phase. In Fig. 8(a), we plot the energy spectrum with the variation of initial phase ϕ_1. One can verify that the energy of the band-gap state satisfies $E_\pm = \pm|J_1|$. We also plot, for one of the band-gap states $|L_-\rangle$, the variation of the distribution with ϕ_1 as shown in Fig. 8(b). It can be seen that if the system is initially prepared to the state $|L_\pm\rangle$ at $\phi_1 = \pi/3$, then this state will be adiabatically evolved to $|R_\pm\rangle$ when we slowly change ϕ_1 to $5\pi/3$.

If the initial state is an arbitrary entangled state $|\Psi_{in}\rangle = (pm^\dagger_{A,1} + qm^\dagger_{B,1})|G\rangle$ at the left end of the chain, it can be written as the superposition of the edge state [75]. For $\phi_1 = \pi/3$, the initial state can be written as

$$|\Psi_{in}\rangle = \frac{p+q}{\sqrt{2}}|L_+\rangle + \frac{p-q}{\sqrt{2}}|L_-\rangle. \quad (13)$$

By slowly changing from $\phi_1 = \pi/3$ to $5\pi/3$, $|L_\pm\rangle$ evolves to $|R_\pm\rangle$. The final state can be written as

$$|\Psi_f\rangle = \frac{p+q}{\sqrt{2}}|R_+\rangle + \frac{p-q}{\sqrt{2}}|R_-\rangle. \quad (14)$$

Substituting the expressions of $|R_\pm\rangle$, we can obtain

$$|\Psi_f\rangle = (pm^\dagger_{A,3M} + qm^\dagger_{B,3M})|G\rangle. \quad (15)$$

Therefore, the arbitrary entanglement state can be transferred from one end to the other end, which actually can be considered as quantum information communication by encoding

quantum information (p, q) in the magnon. Thus, the simulated SSH3 model can be used for long-range quantum communication with the advantage of being insensitive to local disorder and perturbations unless the perturbation induces topological phase transitions. In addition, varying the phase ϕ_1 for the arbitrary state transfer requires slow and adiabatic change, thus ultrafast quantum computing is a challenge for the current system as well as for many other adiabatic processes [70–73,76,77]. In order to accelerate edge state transfer, people have introduced next-nearest-neighbor interactions [78], combining topological pumping of edge states and coherent tunneling of adiabatic channels [79], which also can be applied for the current scheme to overcome the shortage of the adiabatic process.

V. DISCUSSION

We now analyze the feasibility of experiments. Recently, superconducting circuits have received increasing attention based on the flexibility of the parameters and the design ability of the system structure, and have become a well-established platform for the study of quantum simulation [80–82], quantum computing [83], and quantum information processing [84]. Based on this platform, the manipulation and measurement at several quantum qubits, the microwave photon, and magnon levels have also been demonstrated in recent experiments [1,3,14,85–89]. Given the connectivity and tunability of the superconducting devices, a series of physical models have been simulated—for example, the quantum spin model [90,91], the Jaynes-Cummings Hubbard model [92,93], and the Bose-Hubbard model [94,95]. Moreover, in recent years there has been increasing interests in simulating and investigating topological models based on superconducting circuits [69,96–101] such as the SSH model [68–70] and the Rice-Mele model [102].

Our proposed scheme can be implemented in the superconducting circuit, where the coupled cavity arrays can be realized by using coupled superconducting transmission line resonators [93]. Experimentally, a magnon mode coupling to two cavity fields with equal strength has been realized in superconducting circuits [103]. Therefore, our scheme can be implemented in the experiment.

Moreover, our scheme can be easily extended to simulating the SSHm model. For different phase shifts y will result in a different number of sublattices. In other words, if we set $y = \pi/m$, where m is an integer and $m > 1$, then the number of sublattices is m. For example, for $y = \pi/4$, the strength of the coupling exhibits a periodic variation with the period of 4 in the pale blue area of Fig. 3(d). This means that we can implement the transfer of arbitrary entangled states by the SSH4 model, which is analogous to the transfer of entangled states in the SSH3 model.

VI. CONCLUSION

In this paper, we present a scheme for simulating the magnon version of the extended SSH model using hybrid cavity magnon systems. We consider a hybrid cavity magnon array with N sites, where each site contains two cavity modes and one magnon mode. And the two hopping rates between

neighbor cavity fields are assumed as real or complex, respectively. Under large detuning conditions, we adiabatically eliminate the cavity field and obtain the periodic interactions between the magnons, which depend on the phase between adjacent cavity fields. After setting the relationship between the phases of adjacent cavity fields, we obtain the magnon version of the extended SSH model. Employing this model, we investigate the distribution of the edge states as well as the topological phase transition. Finally, considering the noninteger cell case, we discuss the magnon entangled state transfer, and the results show that the arbitrary entangled state transfer can be achieved by slowly and adiabatically changing the phases.

ACKNOWLEDGMENTS

APPENDIX: EFFECTIVE MAGNON-MAGNON COUPLING

In this section, we use Schrieffer-Wolff transformation to adiabatically eliminate the cavity field. The Hamiltonian of the system can be written as the noninteracting part H_0 and the interacting part H_I as

$$H = H_0 + H_I. \tag{A1}$$

Define a similar transformation $U = \exp(S)$, where S is an anti-Hermitian operator $S^\dagger = -S$ [64]. Then, after using Schrieffer-Wolff transformation, the Hamiltonian becomes

$$H_S = UHU^\dagger = H + [S,H] + \frac{1}{2}[S,[S,H]] + \cdots. \tag{A2}$$

One can choose an appropriate S to eliminate the linear dependence on H_I—for example, by setting the term of the first-order perturbation to zero as $H_I + [H_0, S] = 0$. Then, the above equation can be written under the second-order perturbation approximation as

$$H_S = H_0 + \frac{1}{2}[S, H_I]. \tag{A3}$$

Now back to the main text, the Hamiltonian Eq. (4) can be rewritten in terms of the noninteracting Hamiltonian, where

$$H_0 = \sum_k (\omega_a + 2J_a \cos k)c_k^\dagger c_k + (\omega_b + 2J_b \cos k)b_k^\dagger b_k$$
$$+ \sum_j \omega_m m_j^\dagger m_j, \tag{A4}$$

and the interacting Hamiltonian

$$H_I = \sum_{j,k} \left(\frac{g_a e^{-i(kj+\theta_j)}}{\sqrt{N}} c_k^\dagger + \frac{g_b e^{-ikj}}{\sqrt{N}} b_k^\dagger \right) m_j + \text{H.c.}. \tag{A5}$$

We note that since $[S, H_0] = -H_I$, thus, S must contain the term of $c_k^\dagger m_j$, $b_k^\dagger m_j$. Combined with S being an anti-Hermitian operator, we can make the following hypothesis: $S = \sum_{j,k}\{-(\eta_{j,k}c_k + \zeta_{j,k}b_k)m_j^\dagger + (\eta_{j,k}^* c_k^\dagger + \zeta_{j,k}^* b_k^\dagger)m_j\}$. Then, we have

$$H_I + [S, H_0] = \sum_{j,k} \left\{ \left(\frac{g_a}{\sqrt{N}} e^{-i(kj+\theta_j)} c_k + \frac{g_b}{\sqrt{N}} e^{ikj} b_k \right) m_j^\dagger \right.$$
$$+ [(\Delta_{am} - 2J_a \cos k)\eta_{j,k}c_k + (\Delta_{bm}$$
$$\left. - 2J_b \cos k)\zeta_{j,k}b_k]m_j^\dagger + \text{H.c.} \right\} = 0, \tag{A6}$$

where $\Delta_{jm} = \omega_j - \omega_m$ $(j = a, b)$ is the detuning between cavity and magnon. It gives rise to $\eta_{j,k} = \frac{g_a e^{-i(kj+\theta_j)}}{\sqrt{N}(\Delta_{am} - 2J_a \cos k)}$, $\zeta_{j,k} = \frac{g_b e^{ikj}}{\sqrt{N}(\Delta_{bm} - 2J_b \cos k)}$. Due to $\{\eta_{j,k}, \zeta_{j,k}\} \ll 1$, we can keep only the second-order terms and safely omit the higher-order terms. Considering that the cavity field starts in a vacuum state, then the effective Hamiltonian can be reduced to

$$H_S = UHU^\dagger = H_0 + \frac{1}{2}[S, H_I]$$
$$= \sum_j \omega_m m_j^\dagger m_j + \sum_{j,l,k} \frac{1}{N} \left[\left(\frac{g_a^2 e^{i(\theta_j - \theta_l)}}{\Delta_{am} - 2J_a \cos k} \right. \right.$$
$$\left. \left. + \frac{g_b^2}{\Delta_{bm} - 2J_b \cos k} \right) m_j^\dagger m_l e^{i(j-l)k} + \text{H.c.} \right]. \tag{A7}$$

[1] Z.-L. Xiang, S. Ashhab, J. Q. You, and F. Nori, Rev. Mod. Phys. **85**, 623 (2013).

[2] D. Lachance-Quirion, Y. Tabuchi, A. Gloppe, K. Usami, and Y. Nakamura, Appl. Express **12**, 070101 (2019).

[3] D. D. Awschalom, C. R. Du, R. He, F. J. Heremans, A. Hoffmann, J. Hou, H. Kurebayashi, Y. Li, L. Liu, V. Novosad, J. Sklenar, S. E. Sullivan, D. Sun, H. Tang, V. Tyberkevych, C. Trevillian, A. W. Tsen, L. R. Weiss, W. Zhang, X. Zhang *et al.*, IEEE Trans. Quantum Eng. **2**, 5500836 (2021).

[4] A. V. Chumak, V. I. Vasyuchka, A. A. Serga, and B. Hillebrands, Nat. Phys. **11**, 453 (2015).

[5] P. Pirro, V. I. Vasyuchka, A. A. Serga, and B. Hillebrands, Nat. Rev. Mater. **6**, 1114 (2021).

[6] H. Huebl, C. W. Zollitsch, J. Lotze, F. Hocke, M. Greifenstein, A. Marx, R. Gross, and S. T. B. Goennenwein, Phys. Rev. Lett. **111**, 127003 (2013).

[7] Y. Tabuchi, S. Ishino, T. Ishikawa, R. Yamazaki, K. Usami, and Y. Nakamura, Phys. Rev. Lett. **113**, 083603 (2014).

[8] J. A. Haigh, A. Nunnenkamp, A. J. Ramsay, and A. J. Ferguson, Phys. Rev. Lett. **117**, 133602 (2016).

[9] X. Zhang, N. Zhu, C.-L. Zou, and H. X. Tang, Phys. Rev. Lett. **117**, 123605 (2016).

[10] A. Osada, R. Hisatomi, A. Noguchi, Y. Tabuchi, R. Yamazaki, K. Usami, M. Sadgrove, R. Yalla, M. Nomura, and Y. Nakamura, Phys. Rev. Lett. **116**, 223601 (2016).

[11] X. Zhang, C.-L. Zou, L. Jiang, and H. X. Tang, Sci. Adv. **2**, e1501286 (2016).

[12] J. Li, S.-Y. Zhu, and G. S. Agarwal, Phys. Rev. Lett. **121**, 203601 (2018).

[13] X. Zhang, C. L. Zou, N. Zhu, F. Marquardt, L. Jiang, and H. X. Tang, Nat. Commun. **6**, 8914 (2015).

[14] H. Y. Yuan, Y. Cao, A. Kamra, R. A. Duine, and P. Yan, Phys. Rep. **965**, 1 (2022).

[15] Y.-P. Wang, G.-Q. Zhang, D. Zhang, T.-F. Li, C.-M. Hu, and J. Q. You, Phys. Rev. Lett. **120**, 057202 (2018).

[16] Y.-P. Wang, J. W. Rao, Y. Yang, P.-C. Xu, Y. S. Gui, B. M. Yao, J. Q. You, and C.-M. Hu, Phys. Rev. Lett. **123**, 127202 (2019).

[17] L. Bai, M. Harder, Y. P. Chen, X. Fan, J. Q. Xiao, and C.-M. Hu, Phys. Rev. Lett. **114**, 227201 (2015).

[18] Y. Li, T. Polakovic, Y.-L. Wang, J. Xu, S. Lendinez, Z. Zhang, J. Ding, T. Khaire, H. Saglam, R. Divan, J. Pearson, W.-K. Kwok, Z. Xiao, V. Novosad, A. Hoffmann, and W. Zhang, Phys. Rev. Lett. **123**, 107701 (2019).

[19] Z.-X. Liu, H. Xiong, M.-Y. Wu, and Y.-Q. Li, Phys. Rev. A **103**, 063702 (2021).

[20] J. Bourhill, N. Kostylev, M. Goryachev, D. L. Creedon, and M. E. Tobar, Phys. Rev. B **93**, 144420 (2016).

[21] C. Kong, H. Xiong, and Y. Wu, Phys. Rev. Appl. **12**, 034001 (2019).

[22] C. Zhao, R. Peng, Z. Yang, S. Chao, C. Li, Z. Wang, and L. Zhou, Phys. Rev. A **105**, 023709 (2022).

[23] Y. Xiao, X. H. Yan, Y. Zhang, V. L. Grigoryan, C. M. Hu, H. Guo, and K. Xia, Phys. Rev. B **99**, 094407 (2019).

[24] C. Zhao, X. Li, S. Chao, R. Peng, C. Li, and L. Zhou, Phys. Rev. A **101**, 063838 (2020).

[25] Z.-X. Liu, H. Xiong, and Y. Wu, Phys. Rev. B **100**, 134421 (2019).

[26] F.-X. Sun, S.-S. Zheng, Y. Xiao, Q. Gong, Q. He, and K. Xia, Phys. Rev. Lett. **127**, 087203 (2021).

[27] Z.-B. Yang, X.-D. Liu, X.-Y. Yin, Y. Ming, H.-Y. Liu, and R.-C. Yang, Phys. Rev. Appl. **15**, 024042 (2021).

[28] B. Wang, X. Jia, X.-H. Lu, and H. Xiong, Phys. Rev. A **105**, 053705 (2022).

[29] C. Zhao, Z. Yang, R. Peng, J. Yang, C. Li, and L. Zhou, Phys. Rev. Appl. **18**, 044074 (2022).

[30] C. C. Rusconi, M. J. A. Schuetz, J. Gieseler, M. D. Lukin, and O. Romero-Isart, Phys. Rev. A **100**, 022343 (2019).

[31] G. Go, I.-S. Hong, S.-W. Lee, S. K. Kim, and K.-J. Lee, Phys. Rev. B **101**, 134423 (2020).

[32] M. Z. Hasan and C. L. Kane, Rev. Mod. Phys. **82**, 3045 (2010).

[33] L. A. Wray, S. Y. Xu, Y. Xia, Y. S. Hor, D. Qian, A. V. Fedorov, H. Lin, A. Bansil, R. J. Cava, and M. Z. Hasan, Nat. Phys. **6**, 855 (2010).

[34] M. I. Shalaev, W. Walasik, A. Tsukernik, Y. Xu, and N. M. Litchinitser, Nat. Nanotechnol. **14**, 31 (2019).

[35] T. Ozawa, H. M. Price, A. Amo, N. Goldman, M. Hafezi, L. Lu, M. C. Rechtsman, D. Schuster, J. Simon, O. Zilberberg, and I. Carusotto, Rev. Mod. Phys. **91**, 015006 (2019).

[36] W. P. Su, J. R. Schrieffer, and A. J. Heeger, Phys. Rev. Lett. **42**, 1698 (1979).

[37] A. J. Heeger, S. Kivelson, J. R. Schrieffer, and W. P. Su, Rev. Mod. Phys. **60**, 781 (1988).

[38] A. Bansil, H. Lin, and T. Das, Rev. Mod. Phys. **88**, 021004 (2016).

[39] X.-W. Xu, Y.-J. Zhao, H. Wang, A.-X. Chen, and Y.-X. Liu, Front. Phys. **9**, 813801 (2022).

[40] C. C. Wanjura, M. Brunelli, and A. Nunnenkamp, Nat. Commun. **11**, 3149 (2020).

[41] E. J. Meier, F. A. An, and B. Gadway, Nat. Commun. **7**, 13986 (2016).

[42] L. Jin, Phys. Rev. A **96**, 032103 (2017).

[43] Z. Guo, X. Wu, S. Ke, L. Dong, F. Deng, H. Jiang, and H. Chen, New J. Phys. **24**, 063001 (2022).

[44] V. M. Martinez Alvarez and M. D. Coutinho-Filho, Phys. Rev. A **99**, 013833 (2019).

[45] M. Maffei, A. Dauphin, F. Cardano, M. Lewenstein, and P. Massignan, New J. Phys. **20**, 013023 (2018).

[46] D. Xie, W. Gou, T. Xiao, B. Gadway, and B. Yan, npj Quantum Inf. **5**, 55 (2019).

[47] C.-X. Du, N. Xu, L. Du, Y. Zhang, and J.-H. Wu, Opt. Express **29**, 37722 (2021).

[48] M. R. Zirnbauer, J. Math. Phys. **62**, 021101 (2021).

[49] A. Anastasiadis, G. Styliaris, R. Chaunsali, G. Theocharis, and F. K. Diakonos, Phys. Rev. B **106**, 085109 (2022).

[50] P. Delplace, D. Ullmo, and G. Montambaux, Phys. Rev. B **84**, 195452 (2011).

[51] X. Ni, M. Weiner, A. Alù, and A. B. Khanikaev, Nat. Mater. **18**, 113 (2019).

[52] L. Lu, J. D. Joannopoulos, and M. Soljačić, Nat. Phys. **8**, 821 (2014).

[53] N. Y. Yao, C. R. Laumann, A. V. Gorshkov, H. Weimer, L. Jiang, J. I. Cirac, P. Zoller, and M. D. Lukin, Nat. Commun. **4**, 1585 (2013).

[54] Y. Zhang, B. Ren, Y. Li, and F. Ye, Opt. Express **29**, 42827 (2021).

[55] Y. V. Kartashov, A. A. Arkhipova, S. A. Zhuravitskii, N. N. Skryabin, I. V. Dyakonov, A. A. Kalinkin, S. P. Kulik, V. O. Kompanets, S. V. Chekalin, L. Torner, and V. N. Zadkov, Phys. Rev. Lett. **128**, 093901 (2022).

[56] N. Huda and S. Kezilebieke, npj Quantum Mater. **5**, 17 (2020).

[57] Z. Zhang, M. H. Teimourpour, J. Arkinstall, M. Pan, P. Miao, H. Schomerus, R. El-Ganainy, and L. Feng, Laser Photonics Rev. **13**, 1800202 (2019).

[58] M. Ezawa, Phys. Rev. B **103**, 155425 (2021).

[59] D. Porras and S. Fernández-Lorenzo, Phys. Rev. Lett. **122**, 143901 (2019).

[60] B. Peropadre, D. Zueco, F. Wulschner, F. Deppe, A. Marx, R. Gross, and J. J. García-Ripoll, Phys. Rev. B **87**, 134504 (2013).

[61] R. Peng, C. Zhao, Z. Yang, J. Yang, and L. Zhou, Phys. Rev. A **107**, 013507 (2023).

[62] K. Fang, Z. Yu, and S. Fan, Nat. Photonics **6**, 782 (2012).

[63] P. Roushan, C. Neill, A. Megrant, Y. Chen, R. Babbush, R. Barends, B. Campbell, Z. Chen, B. Chiaro, A. Dunsworth, A. Fowler, E. Jeffrey, J. Kelly, E. Lucero, J. Mutus, P. J. O'Malley, M. Neeley, C. Quintana, D. Sank, A. Vainsencher *et al.*, Nat. Phys. **13**, 146 (2017).

[64] J. R. Schrieffer and P. A. Wolff, Phys. Rev. **149**, 491 (1966).

[65] S. Yao and Z. Wang, Phys. Rev. Lett. **121**, 086803 (2018).

[66] H. Ghaemi-Dizicheh and H. Schomerus, Phys. Rev. A **104**, 023515 (2021).

[67] W.-T. Xue, M.-R. Li, Y.-M. Hu, F. Song, and Z. Wang, Phys. Rev. B **103**, L241408 (2021).

[68] D.-W. Wang, C.-S. Zhao, S.-L. Chao, R. Peng, J. Yang, Z. Yang, and L. Zhou, Opt. Express **30**, 42347 (2022).

[69] W. Nie, Z. H. Peng, F. Nori, and Y.-X. Liu, Phys. Rev. Lett. **124**, 023603 (2020).

[70] N. Lang and H. P. Büchler, npj Quantum Inf. **3**, 47 (2017).

[71] F. Mei, G. Chen, L. Tian, S.-L. Zhu, and S. Jia, Phys. Rev. A **98**, 012331 (2018).

[72] L. Qi, G.-L. Wang, S. Liu, S. Zhang, and H.-F. Wang, Phys. Rev. A **102**, 022404 (2020).

[73] J. Cao, W.-X. Cui, X. X. Yi, and H.-F. Wang, Phys. Rev. A **103**, 023504 (2021).

[74] Y. He, K. Wright, S. Kouachi, and C.-C. Chien, Phys. Rev. A **97**, 023618 (2018).

[75] C. Wang, L. Li, J. Gong, and Y.-X. Liu, Phys. Rev. A **106**, 052411 (2022).

[76] S. Longhi, G. L. Giorgi, and R. Zambrini, Adv. Quantum Technol. **2**, 1800090 (2019).

[77] N. E. Palaiodimopoulos, I. Brouzos, F. K. Diakonos, and G. Theocharis, Phys. Rev. A **103**, 052409 (2021).

[78] F. M. D'Angelis, F. A. Pinheiro, D. Guéry-Odelin, S. Longhi, and F. Impens, Phys. Rev. Res. **2**, 033475 (2020).

[79] S. Longhi, Phys. Rev. B **99**, 155150 (2019).

[80] I. Buluta and F. Nori, Science **326**, 108 (2009).

[81] M. Fitzpatrick, N. M. Sundaresan, A. C. Y. Li, J. Koch, and A. A. Houck, Phys. Rev. X **7**, 011016 (2017).

[82] C. Noh and D. G. Angelakis, Rep. Prog. Phys. **80**, 016401 (2017).

[83] A. J. Daley, I. Bloch, C. Kokail, S. Flannigan, N. Pearson, M. Troyer, and P. Zoller, Nature (London) **607**, 667 (2022).

[84] A. Blais, J. Gambetta, A. Wallraff, D. I. Schuster, S. M. Girvin, M. H. Devoret, and R. J. Schoelkopf, Phys. Rev. A **75**, 032329 (2007).

[85] D. Vion, A. Aassime, A. Cottet, P. Joyez, H. Pothier, C. Urbina, D. Esteve, and M. H. Devoret, Science **296**, 886 (2002).

[86] A. A. Houck, H. E. Türeci, and J. Koch, Nat. Phys. **8**, 292 (2012).

[87] S. Schmidt and J. Koch, Ann. Phys. **525**, 395 (2013).

[88] Z. Wang, T. Jaako, P. Kirton, and P. Rabl, Phys. Rev. Lett. **124**, 213601 (2020).

[89] B. Kannan, M. J. Ruckriegel, D. L. Campbell, A. Frisk Kockum, J. Braumüller, D. K. Kim, M. Kjaergaard, P. Krantz, A. Melville, B. M. Niedzielski, A. Vepsäläinen, R. Winik, J. L. Yoder, F. Nori, T. P. Orlando, S. Gustavsson, and W. D. Oliver, Nature (London) **583**, 775 (2020).

[90] U. L. Heras, A. Mezzacapo, L. Lamata, S. Filipp, A. Wallraff, and E. Solano, Phys. Rev. Lett. **112**, 200501 (2014).

[91] O. Viehmann, J. von Delft, and F. Marquardt, Phys. Rev. Lett. **110**, 030601 (2013).

[92] K. Seo and L. Tian, Phys. Rev. B **91**, 195439 (2015).

[93] A. Blais, A. L. Grimsmo, S. M. Girvin, and A. Wallraff, Rev. Mod. Phys. **93**, 025005 (2021).

[94] M. J. Hartmann, J. Opt. **18**, 104005 (2016).

[95] L.-L. Zheng, K.-M. Li, X.-Y. Lü, and Y. Wu, Phys. Rev. A **96**, 053809 (2017).

[96] M. Bello, G. Platero, J. I. Cirac, and A. González-Tudela, Sci. Adv. **5**, eaaw0297 (2019).

[97] L. Leonforte, A. Carollo, and F. Ciccarello, Phys. Rev. Lett. **126**, 063601 (2021).

[98] E. Kim, X. Zhang, V. S. Ferreira, J. Banker, J. K. Iverson, A. Sipahigil, M. Bello, A. González-Tudela, M. Mirhosseini, and O. Painter, Phys. Rev. X **11**, 011015 (2021).

[99] M. Bello, G. Platero, and A. González-Tudela, PRX Quantum **3**, 010336 (2022).

[100] C. Vega, M. Bello, D. Porras, and A. González-Tudela, Phys. Rev. A **104**, 053522 (2021).

[101] F. Mei, G. Chen, L. Tian, S.-L. Zhu, and S. Jia, Phys. Rev. A **98**, 032323 (2018).

[102] L. Qi, Y. Xing, X.-D. Zhao, S. Liu, S. Zhang, S. Hu, and H.-F. Wang, Phys. Rev. B **103**, 085129 (2021).

[103] J. W. Rao, S. Kaur, B. M. Yao, E. R. Edwards, Y. T. Zhao, X. Fan, D. Xue, T. J. Silva, Y. S. Gui, and C.-M. Hu, Nat. Commun. **10**, 2934 (2019).